Published by Institute of Physics Publishing for SISSA

Received: *December 11, 2007*
Accepted: *January 24, 2008*
Published: *February 6, 2008*

Hadronic production of top-squark pairs with electroweak NLO contributions

Wolfgang Hollik, Monika Kollár and Maike K. Trenkel

Max-Planck-Institut für Physik,
Föhringer Ring 6, D-80805 München, Germany
E-mail: hollik@mppmu.mpg.de, monika.kollar@mppmu.mpg.de, trenkel@mppmu.mpg.de

Abstract: Presented are complete next-to-leading order electroweak (NLO EW) corrections to top-squark pair production at the Large Hadron Collider (LHC) within the Minimal Supersymmetric Standard Model (MSSM). At this order, also effects from the interference of EW and QCD contributions have to be taken into account. Moreover, photon-induced top-squark production is considered as an additional partonic channel, which arises from the non-zero photon density in the proton.

Keywords: Supersymmetric Standard Model, NLO Computations, Hadronic Colliders.

JHEP02(2008)018

Contents

1. Introduction

Within supersymmetric theories top-squarks are the supersymmetric partners of the left- and right-handed top quarks. The two superpartners $\tilde{t}_L$ and $\tilde{t}_R$, which belong to chiral supermultiplets $\hat{Q}$ and $\hat{T}$, in general mix to produce two mass eigenstates $\tilde{t}_1$ and $\tilde{t}_2$. In many supersymmetric models the lighter mass eigenstate appears as the lightest colored sparticle [1], for reasons related to the large top Yukawa coupling. The large mixing in the stop sector leads to a substantial splitting between the two mass eigenstates, and the evolution from the GUT scale to the electroweak scale yields low values for the stop masses when a universal scalar mass is assumed at the high scale [2]. The search for top-squarks is therefore of particular interest for the coming LHC experiments, where they would be primarily produced in pairs via the strong interaction, with relatively large cross sections.

Current experimental limits on top-squark pair production include searches performed at LEP [3 – 6] reviewed e.g in [7], and at the Tevatron, done by the CDF and DØ collaborations in approximately 90 pb^{-1} of Run I data [8, 9]. Extended searches have been done using Run II data samples by both CDF and DØ [10 – 12]. Limits on the top-squark mass, depending on the mass of the lightest neutralino, are provided with the assumption that $BR(\tilde{t}_1 \to c\tilde{\chi}_1^0) = 100$ % in [13].

Experimental searches for the top-squarks have also been done in ep collisions at HERA [14, 15], where only single stop production could be kinematically accessed and hence constraints have been derived essentially on the R-parity violating class of supersymmetric models.

Concerning the theoretical predictions, QCD-based Born-level cross sections for the production of squarks and gluinos in hadron collisions have been calculated in [16 − 20]. They have been improved by including NLO corrections in supersymmetric QCD (SUSY-QCD), worked out in [21, 22] with the restriction to final state squarks of the first two generations, and for the stop sector in [23]. The production of top-squark pairs in hadronic collisions is diagonal at lowest order at $\mathcal{O}(\alpha_s^2)$. Electroweak (EW) contributions of $\mathcal{O}(\alpha^2)$ are suppressed by two orders of magnitude. Also at $\mathcal{O}(\alpha_s^3)$ the production mechanism is still diagonal. Non-diagonal production occurs at $\mathcal{O}(\alpha_s^4)$, and the cross section is accordingly suppressed. Production of non-diagonal top-squark pairs can also proceed at $\mathcal{O}(\alpha^2)$ mediated by Z-exchange through $q\overline{q}$ annihilation [24] as well as in e^+e^- annihilation [25].

The LO cross section for diagonal top-squark pair production depends only on the mass of the produced squarks. As a consequence, bounds on the production cross section can easily be translated into lower bounds on the lightest stop mass. At NLO, the cross section becomes considerably changed and dependent on other supersymmetric parameters, like mixing angles, gluino mass, masses of other squarks, etc., which enter through the higher order terms. Once top-squarks are discovered, measurement of their masses and cross sections will provide important observables for testing and constraining the supersymmetric model.

In the following, we study the NLO contributions to diagonal top-squark pair production that arise from the electroweak interaction within the Minimal Supersymmetric Standard Model (MSSM). We assume the MSSM with real parameters, R-parity conservation, and minimal flavor violation. The outline of our paper is as follows. In section 2, we present analytical expressions for the partonic and hadronic LO cross sections. We also introduce some basic notations used throughout the paper. Section 3 is dedicated to the classification of the NLO EW contributions into virtual and real corrections with the treatment of soft and collinear singularities, and photon-induced contributions. In section 4, we give a list of input parameters and conventions, followed by our numerical results for the hadronic cross sections and distributions for pp collisions at a center-of-mass energy $\sqrt{S} = 14$ TeV at the LHC. We also investigate the application of kinematical cuts, and we analyze the impact of varying the MSSM parameters.

2. Top-squark eigenstates and LO cross sections

In the MSSM Lagrangian, mixing of the left- and right-handed top-squark eigenstates $\tilde{t}_{L/R}$ into mass eigenstates $\tilde{t}_{1/2}$ is induced by the trilinear Higgs-stop-stop coupling term A_t and the Higgs-mixing parameter μ. The top-squark mass matrix squared is given by [26]

$$\mathfrak{M}^2 = \begin{pmatrix} m_t^2 + A_{LL} & m_t B_{LR} \\ m_t B_{LR} & m_t^2 + C_{RR} \end{pmatrix}, \tag{2.1}$$

with m_t denoting the top-quark mass and

$$\begin{aligned} A_{LL} &= \left(\frac{1}{2} - \frac{2}{3}\sin^2\theta_W\right) m_Z^2 \cos 2\beta + m_{\tilde{Q}_3}^2 \,, \\ B_{LR} &= A_t - \mu \cot\beta \,, \\ C_{RR} &= \frac{2}{3}\sin^2\theta_W\, m_Z^2 \cos 2\beta + m_{\tilde{U}_3}^2 \,. \end{aligned} \tag{2.2}$$

Here, $\tan\beta$ is the ratio of the vacuum expectation values of the two Higgs doublets and $m_{\tilde{Q}_3}$, $m_{\tilde{U}_3}$ are the soft-breaking mass terms for left- and right-handed top-squarks, respectively.

The top-squark mass eigenvalues are obtained by diagonalizing the mass matrix,

$$U\mathfrak{M}^2 U^\dagger = \begin{pmatrix} m_{\tilde{t}_1}^2 & 0 \\ 0 & m_{\tilde{t}_2}^2 \end{pmatrix}, \qquad U = \begin{pmatrix} \cos\theta_{\tilde{t}} & \sin\theta_{\tilde{t}} \\ -\sin\theta_{\tilde{t}} & \cos\theta_{\tilde{t}} \end{pmatrix}, \tag{2.3}$$

$$m_{\tilde{t}_{1,2}}^2 = m_t^2 + \frac{1}{2}\left(A_{LL} + C_{RR} \mp \sqrt{(A_{LL} - C_{RR})^2 + 4m_t^2 B_{LR}^2}\right), \tag{2.4}$$

and the mixing angle $\theta_{\tilde{t}}$ is determined by

$$\tan 2\theta_{\tilde{t}} = \frac{2m_t B_{LR}}{A_{LL} - C_{RR}}. \tag{2.5}$$

At hadron colliders, diagonal pairs of top-squarks can be produced at leading order in QCD in two classes of partonic subprocesses,

$$\begin{aligned} gg &\to \tilde{t}_1\,\tilde{t}_1^* \quad \text{and} \quad \tilde{t}_2\,\tilde{t}_2^*, \\ q\bar{q} &\to \tilde{t}_1\,\tilde{t}_1^* \quad \text{and} \quad \tilde{t}_2\,\tilde{t}_2^*\,, \end{aligned} \tag{2.6}$$

where $q\bar{q}$ denotes representatively the contributing quark flavors. The corresponding Feynman diagrams for the example of $\tilde{t}_1\,\tilde{t}_1^*$ production are shown in the appendix, figure 12. As already mentioned, mixed pairs cannot be produced at lowest order since the $g\,\tilde{t}\tilde{t}^*$ and $gg\,\tilde{t}\tilde{t}^*$ vertices are diagonal in the chiral as well as in the mass basis.

The differential partonic cross sections for the subprocesses,

$$d\hat{\sigma}_0^{gg,q\bar{q}}(\hat{s}) = \frac{1}{16\pi\hat{s}^2}\overline{\sum}\left|\mathcal{M}_0^{gg,q\bar{q}}(\hat{s},\hat{t},\hat{u})\right|^2 d\hat{t}\,, \tag{2.7}$$

can be expressed in terms of the squared and spin-averaged lowest-order matrix elements, as explicitly given by [21, 22],

$$\overline{\sum}|\mathcal{M}_0^{gg}|^2 = \frac{1}{4}\cdot\frac{1}{64}\cdot 32\pi^2\alpha_s^2\left[C_0\left(1 - 2\frac{\hat{t}_r\,\hat{u}_r}{\hat{s}^2}\right) - C_K\right]\left[1 - 2\frac{\hat{s}m_{\tilde{t}_i}^2}{\hat{t}_r\,\hat{u}_r}\left(1 - \frac{\hat{s}m_{\tilde{t}_i}^2}{\hat{t}_r\,\hat{u}_r}\right)\right], \tag{2.8}$$

$$\overline{\sum}|\mathcal{M}_0^{q\bar{q}}|^2 = \frac{1}{4}\cdot\frac{1}{9}\cdot 64\pi^2\alpha_s^2\, NC_F\,\frac{\hat{t}_r\,\hat{u}_r - m_{\tilde{t}_i}^2\,\hat{s}}{\hat{s}^2}, \tag{2.9}$$

with $\hat{t}_r = \hat{t} - m_{\tilde{t}_i}^2$, $\hat{u}_r = \hat{u} - m_{\tilde{t}_i}^2$, where $\hat{s}$, $\hat{t}$, $\hat{u}$ are the usual Mandelstam variables. $i = 1, 2$ denotes the two mass eigenstates. The SU(3) color factors are given by $N = 3$, $C_0 = N(N^2-1) = 24$, $C_K = (N^2-1)/N = 8/3$ and $C_F = (N^2-1)/(2N) = 4/3$.

The differential cross section at the hadronic level for the process $AB \to \tilde{t}_i \tilde{t}_i^*$, i =1, 2, is related to the partonic cross sections through

$$d\sigma^{AB}(S) = \sum_{a,b} \int_{\tau_0}^{1} d\tau \, \frac{d\mathcal{L}_{ab}^{AB}}{d\tau} \, d\hat{\sigma}_0^{ab}(\hat{s}) \,, \tag{2.10}$$

with $\tau = \hat{s}/S$, S ($\hat{s}$) being the hadronic (partonic) center-of-mass energy squared and $\tau_0 = 4m_{\tilde{t}_i}^2/S$ is the production threshold. The sum over a, b runs over all possible initial partons. The parton luminosities are given by

$$\frac{d\mathcal{L}_{ab}^{AB}}{d\tau} = \frac{1}{1+\delta_{ab}} \int_{\tau}^{1} \frac{dx}{x} \left[f_{a/A}(x, \mu_F) \, f_{b/B}\Big(\frac{\tau}{x}, \mu_F\Big) + f_{b/A}\Big(\frac{\tau}{x}, \mu_F\Big) \, f_{a/B}(x, \mu_F) \right], \tag{2.11}$$

where the parton distribution functions (PDFs) $f_{a/A}(x, \mu_F)$ parameterize the probability of finding a parton a inside a hadron A with fraction x of the hadron momentum at a factorization scale μ_F.

3. Classification of EW NLO corrections

In the following we describe the calculation of EW contributions to top-squark pair production at NLO. For the treatment of the Feynman diagrams and corresponding amplitudes we make use of `FeynArts 3.2` [27 – 29] and `FormCalc 5.2` with `LoopTools 2.2` [30, 31], based on Passarino-Veltman reduction techniques for the tensor loop integrals [32, 33], which were further developed for 4-point integrals in [34, 35]. Higgs properties are computed with `FeynHiggs 2.5.1` [36, 37].

The supersymmetric final state does not allow to separate the SM-like corrections from the superpartner contributions which are necessary for the cancellation of ultra-violet (UV) singularities. As the photino is not a mass eigenstate of the theory, it is also not possible to split the EW corrections into a QED and a weak part, which is often the case in SM processes. In order to obtain a UV finite result, we have to deal with the complete set of EW virtual corrections including photonic contributions. These are infrared (IR) singular and thus also the real photonic corrections have to be taken into account. In addition, a photon-induced subclass of corrections appears at NLO as an independent production channel.

3.1 Virtual corrections

The virtual corrections arise from self-energy, vertex, box, and counter-term diagrams. These are shown in the appendix, in figure 13 for the $q\overline{q}$ annihilation and and in figure 14 for the gluon fusion channel, respectively. Getting an UV finite result requires renormalization of the involved quarks and top-squarks. The renormalized quark and squark self-energies are obtained from the unrenormalized initial quark self-energies

$$\Sigma^q(\not{p}) = \not{p}\omega_- \Sigma_L^q(p^2) + \not{p}\omega_+ \Sigma_R^q(p^2) + m_q \Sigma_S^q(p^2), \tag{3.1}$$

according to

$$
\begin{aligned}
\hat{\Sigma}^q_L(p^2) &= \Sigma^q_L(p^2) + \delta Z^q_L\,, \\
\hat{\Sigma}^q_R(p^2) &= \Sigma^q_R(p^2) + \delta Z^q_R\,, \\
\hat{\Sigma}^q_S(p^2) &= \Sigma^q_S(p^2) - \frac{1}{2}\left(\delta Z^q_L + \delta Z^q_R\right) + \frac{\delta m_q}{m_q}\,,
\end{aligned}
\tag{3.2}
$$

and from the top-squark self-energies $\Sigma_{\tilde{t}_i}(k^2)$ (for i =1, 2), according to

$$
\hat{\Sigma}_{\tilde{t}_i}(k^2) = \Sigma_{\tilde{t}_i}(k^2) + k^2\delta Z_{\tilde{t}_i} - m^2_{\tilde{t}_i}\delta Z_{\tilde{t}_i} - \delta m^2_{\tilde{t}_i}\,,
\tag{3.3}
$$

with the renormalized quantities denoted by the symbol $\hat{\Sigma}$.

The full set of virtual contributions is UV finite after including the proper counter-terms for self-energies, quark vertices, and squark triple and quartic vertices, as listed in the following set of Feynman rules:

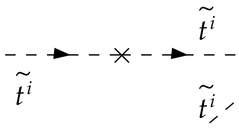

$$
i\delta\Sigma_{\tilde{t}_i} = i\left(k^2\,\delta Z_{\tilde{t}_i} - m^2_{\tilde{t}_i}\delta Z_{\tilde{t}_i} - \delta m^2_{\tilde{t}_i}\right)\,,
\tag{3.4}
$$

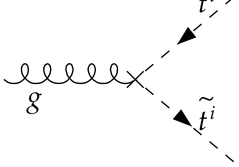

$$
i\delta\Lambda_{\mu_i} = -ig_sT^c\left(k+k'\right)_\mu\,\delta Z_{\tilde{t}_i}\,,
\tag{3.5}
$$

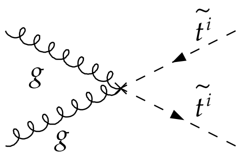

$$
i\delta\Lambda^{SSVV}_{\mu_i} = \frac{1}{2}ig_s^2\left(\frac{1}{3}\delta_{ab} + d_{abc}T^c\right)g_{\mu\nu}\,\delta Z_{\tilde{t}_i}\,,
\tag{3.6}
$$

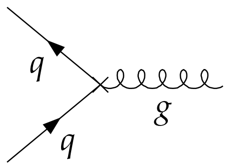

$$
i\delta\Lambda^q_\mu = -ig_sT^c\gamma_\mu\,\left(\omega_-\delta Z^q_L + \omega_+\delta Z^q_R\right)\,,
\tag{3.7}
$$

where k, k' denote the momenta of top-squarks (in the direction of arrows), a, b, and c are the gluonic color indices, T^c and d_{abc} are the color factors (we skip the fermionic and sfermionic color indices), and $\omega_\pm = (1\pm\gamma_5)/2$ are the projection operators. The renormalization constants are fixed within the on-shell renormalization scheme as follows,

$$
\delta m^2_{\tilde{t}_i} = \quad \mathrm{Re}\,\Sigma_{\tilde{t}_i}(m^2_{\tilde{t}_i})\,,
\tag{3.8}
$$

$$
\delta Z_{\tilde{t}_i} = -\,\frac{d}{dk^2}\mathrm{Re}\,\Sigma_{\tilde{t}_i}(k^2)\Big|_{k^2=m^2_{\tilde{t}_i}}\,,
\tag{3.9}
$$

$$
\delta Z^q_{L,R} = -\,\mathrm{Re}\,\Sigma^q_{L,R}(m_q^2) - m_q^2\frac{\partial}{\partial p^2}\mathrm{Re}\left[\Sigma^q_L(p^2) + \Sigma^q_R(p^2) + 2\Sigma^q_S(p^2)\right]\Big|_{p^2=m_q^2}\,.
\tag{3.10}
$$

There is no renormalization of the gluon field at $\mathcal{O}(\alpha)$. Also, the strong coupling constant does not need renormalization since UV singularities cancel in the sum of 3- and 4-point functions and their corresponding counter-terms from quark and squark field renormalization (see figures 13 a and 14 a in the appendix).

Loop diagrams involving virtual photons generate IR singularities. According to Bloch-Nordsieck [38], IR singular terms cancel against their counterparts in the real photon corrections. To regularize the IR singularities we introduce a fictitious photon mass λ. In case of external light quarks, also collinear singularities occur if a photon is radiated off a massless quark in the collinear limit. We therefore keep non-zero initial-state quark masses m_q in the loop integrals. This gives rise to single and double logarithmic contributions of quark masses. The double logarithms cancel in the sum of virtual and real corrections, single logarithms, however, survive and have to be treated by means of the factorization.

In the gg fusion channel, IR singularities originate only from final-state photon radiation, and mass singularities do not occur. In the $q\overline{q}$ annihilation subprocess, the IR singular structure is extended by the contributions related to the gluons which appear in the 4-point UV finite loop integrals. There are two types of IR singular box contributions (figure 13 c). The first group is formed by the gluon-photon box diagrams with two sources of IR singularities, one related to photons, the other to gluons. The second group consists of the gluon–Z box diagrams with IR singularities originating from the gluons only. There is also an IR finite group of $\mathcal{O}(\alpha\alpha_\mathrm{s})$ box diagrams which consists of gluino-neutralino loops (figure 13 d). Owing to the photon-like appearance of the gluon in the box contributions, the gluonic IR singularities can be handled in analogy to the photon IR singularities.

3.2 Real corrections

To compensate IR singularities in the virtual EW corrections, contributions with real photon (figure 15 a and c) and real gluon radiation are required. In case of gg fusion, only photon bremsstrahlung is needed, whereas in the $q\overline{q}$ annihilation channel, also gluon bremsstrahlung at the appropriate order $\mathcal{O}(\alpha\alpha_\mathrm{s}^2)$ has to be taken into account (figure 16) to cancel the IR singularities related to the gluon. The necessary contributions originate from the interference of QCD and EW Born level diagrams, which vanishes at LO. Not all of the interference terms contribute. Due to the color structure, only the interference between initial and final state gluon radiation is non-zero.

Including the EW-QCD interference in the real corrections does not yet lead to an IR finite result. Also the IR singular QCD-mediated box corrections interfering with the $\mathcal{O}(\alpha)$ photon and Z-boson tree-level diagrams are needed. Besides the gluonic corrections there are also the IR finite QCD-mediated box corrections, which contain gluinos in the loop. Interfered with the $\mathcal{O}(\alpha)$ tree-level diagrams, these also give contributions of the respective order of $\mathcal{O}(\alpha\alpha_\mathrm{s}^2)$. The set of all $\mathcal{O}(\alpha_\mathrm{s}^2)$ diagrams is shown in figure 17.

So far we have mentioned only the IR singular bremsstrahlung contributions. However, there are also IR finite real corrections to both gluon fusion and $q\overline{q}$ annihilation processes. In addition to the photon radiation off the off-shell top-squark there are photon radiation contributions originating from the quartic gluon-photon-squark-squark coupling. These contributions do not have to be regularized since they are not singular (figure 15 b and d).

The treatment of IR singular bremsstrahlung is done using the phase space slicing method. Imposing cut-offs ΔE on the photon/gluon energy and $\Delta\theta$ on the angle between the photon/gluon and radiating fermion, the photonic/gluonic phase space is split into soft and collinear parts which contain singularities and a non-collinear, hard part which is free of singularities and is integrated numerically. The sum of virtual and real contributions, each of them dependent on the cut-off parameters ΔE and $\Delta\theta$, has to provide a fully independent result. To ensure this we perform numerical checks (see the discussion in section 4.1).

In the singular regions, the squared matrix elements for the radiative processes factorize into the lowest-order squared matrix elements and universal factors containing the singularities.

3.2.1 Soft singularities

The soft-photon part of the radiative cross section in the $q\overline{q}$ annihilation channel

$$d\hat{\sigma}^{q\overline{q}}_{\mathrm{soft},\gamma}(\hat{s}) = \frac{\alpha}{\pi}\left(e_q^2\,\delta^{\mathrm{in}}_{\mathrm{soft}} + e_t^2\,\delta^{\mathrm{fin}}_{\mathrm{soft}} + 2e_q e_t\,\delta^{\mathrm{int}}_{\mathrm{soft}}\right) d\hat{\sigma}^{q\overline{q}}_0(\hat{s})\,, \tag{3.11}$$

and in the gg fusion channel

$$d\hat{\sigma}^{gg}_{\mathrm{soft},\gamma}(\hat{s}) = \frac{\alpha}{\pi}\,e_t^2\,\delta^{\mathrm{fin}}_{\mathrm{soft}}\,d\hat{\sigma}^{gg}_0(\hat{s})\,, \tag{3.12}$$

can be expressed using universal factors, $\delta^{\mathrm{in,fin,int}}_{\mathrm{soft}}$, which refer to the initial state radiation, final state radiation or interference of initial and final state radiation, respectively. $d\hat{\sigma}_0^{q\overline{q},gg}$ denote the corresponding partonic lowest order cross sections. The singular universal factors, similar to those in [39], read as follows,

$$\begin{aligned}
\delta^{\mathrm{in}}_{\mathrm{soft}} &= \left[\ln\delta_s^2 - \ln\frac{\lambda^2}{\hat{s}}\right]\left[\ln\frac{\hat{s}}{m_q^2} - 1\right] - \frac{1}{2}\ln^2\frac{\hat{s}}{m_q^2} + \ln\frac{\hat{s}}{m_q^2} - \frac{\pi^2}{3}\,,\\
\delta^{\mathrm{fin}}_{\mathrm{soft}} &= \left[\ln\delta_s^2 - \ln\frac{\lambda^2}{\hat{s}}\right]\left[\frac{\hat{s}-2m^2_{\tilde{t}_i}}{\hat{s}\beta}\ln\left(\frac{1+\beta}{1-\beta}\right) - 1\right] + \frac{1}{\beta}\ln\left(\frac{1+\beta}{1-\beta}\right)\\
&\quad - \frac{\hat{s}-2m^2_{\tilde{t}_i}}{\hat{s}\beta}\left[2\mathrm{Li}_2\left(\frac{2\beta}{1+\beta}\right) + \frac{1}{2}\ln^2\left(\frac{1+\beta}{1-\beta}\right)\right],\\
\delta^{\mathrm{int}}_{\mathrm{soft}} &= \left[\ln\delta_s^2 - \ln\frac{\lambda^2}{\hat{s}}\right]\ln\left(\frac{1-\beta\cos\theta}{1+\beta\cos\theta}\right) - \mathrm{Li}_2\left(1 - \frac{1-\beta}{1-\beta\cos\theta}\right)\\
&\quad - \mathrm{Li}_2\left(1 - \frac{1+\beta}{1-\beta\cos\theta}\right) + \mathrm{Li}_2\left(1 - \frac{1-\beta}{1+\beta\cos\theta}\right) + \mathrm{Li}_2\left(1 - \frac{1+\beta}{1+\beta\cos\theta}\right).
\end{aligned} \tag{3.13}$$

Here, e_q and e_t are the electric charges of the initial quark and of the top-squark, respectively, and we introduced $\delta_s = 2\Delta E/\sqrt{\hat{s}}$, where ΔE is the slicing parameter for the maximum energy a soft photon may have. For application purposes, it is useful to express eq. (3.13) in terms of Mandelstam invariants, $\hat{t}$ and $\hat{u}$, using the relations

$$\hat{t},\,\hat{u} = m^2_{\tilde{t}_i} - \frac{\hat{s}}{2}\left(1 \mp \beta\cos\theta\right), \qquad \beta = \sqrt{1 - \frac{4m_{\tilde{t}_i}}{\hat{s}}}. \tag{3.14}$$

The soft-gluon part for the $q\bar{q}$ channel can be written in a way similar to (3.11), but with a different arrangement of the color matrices,

$$\begin{aligned} d\hat{\sigma}^{q\bar{q}}_{\mathrm{soft},g}(\hat{s}) = \frac{\alpha_s}{\pi}\, \delta^{\mathrm{int}}_{\mathrm{soft}} & \left[T^a_{ij}T^b_{ji}T^a_{lm}T^b_{ml}\right] \\ & \times 2\,\mathrm{Re}\overline{\sum}\left(\widetilde{\mathcal{M}}^{q\bar{q}\,*}_{0,g}\widetilde{\mathcal{M}}^{q\bar{q}}_{0,\gamma} + \widetilde{\mathcal{M}}^{q\bar{q}\,*}_{0,g}\widetilde{\mathcal{M}}^{q\bar{q}}_{0,Z}\right)\frac{d\hat{t}}{16\pi\hat{s}^2}\,, \end{aligned} \tag{3.15}$$

with $\widetilde{\mathcal{M}}$ denoting the "Born" matrix elements for g, γ and Z exchange where the color matrices are factorized off. Explicitly, it can be written as follows,

$$\begin{aligned} d\hat{\sigma}^{q\bar{q}}_{\mathrm{soft},g}(\hat{s}) = \frac{\alpha_s}{\pi}\, \delta^{\mathrm{int}}_{\mathrm{soft}}\, N C_F & \left[\frac{8e_q e_t}{\hat{s}^2} + \frac{\left((U_{1i})^2 - 2e_t\sin^2\theta_W\right)\left(\epsilon - 4e_q\sin^2\theta_W\right)}{\sin^2\theta_W\cos^2\theta_W\,\hat{s}(\hat{s}-m_Z^2)}\right] \\ \times \frac{16\pi^2\alpha\alpha_s}{4\cdot 9} & \left[\left(\hat{t}-m^2_{\tilde{t}_i}\right)\left(\hat{u}-m^2_{\tilde{t}_i}\right) - m^2_{\tilde{t}_i}\hat{s}\right]\frac{d\hat{t}}{16\pi\hat{s}^2}\,, \end{aligned} \tag{3.16}$$

involving the top-squark mixing matrix of eq. (2.4), and $\epsilon = \pm 1$ for up- and down-type initial quarks, respectively.

3.2.2 Collinear singularities

Collinear singularities arise only from initial-state photon radiation in $q\bar{q}$ annihilation. The collinear part of the $2 \to 3$ cross section is proportional to the Born cross section of the hard process with reduced momentum of one of the partons. Assuming that parton a with momentum p_a radiates off a photon with $p_\gamma = (1-z)p_a$, the parton momentum available for the hard process is reduced to zp_a. Accordingly, the partonic energy of the total process inclusive photon radiation is $\tilde{s} = (p_a + p_b)^2 = \tilde{\tau}S$, and for the hard process the reduced partonic energy is $\hat{s} = (zp_a + p_b)^2 = \tau S$. The 'total' and 'hard' variables are thus related by $\hat{s} = z\tilde{s}$ and $\tau = z\tilde{\tau}$.

Having defined these variables, the partonic cross section in the collinear cones can be written in the following way [40, 41]

$$\begin{aligned} d\hat{\sigma}_{\mathrm{coll}}(\hat{s}) &= \frac{\alpha}{\pi}\, e_q^2 \int_0^{1-\delta_s} dz\; d\hat{\sigma}^{q\bar{q}}_0(\hat{s})\; \kappa_{\mathrm{coll}}(z) \quad , \\ \text{with} \qquad \kappa_{\mathrm{coll}}(z) &= \frac{1}{2}P_{qq}(z)\left[\ln\left(\frac{\tilde{s}}{m_q^2}\frac{\delta_\theta}{2}\right) - 1\right] + \frac{1}{2}(1-z), \end{aligned} \tag{3.17}$$

where $P_{qq}(z) = (1+z^2)/(1-z)$ is an Altarelli-Parisi splitting function [42] and δ_θ is the cut-off parameter to define the collinear region by $\cos\theta > 1 - \delta_\theta$. The Born cross section refers to the hard scale $\hat{s}$, whereas in the collinear factor the total energy $\tilde{s}$ is the scale needed. In order to avoid an overlap with the soft region, the upper limit of the z-integration in eq. (3.17) is reduced from $z = 1$ to $z = 1 - \delta_s$.

As already mentioned, after adding virtual and real corrections, the mass singularity in eq. (3.17) does not cancel and has to be absorbed into the (anti-)quark density functions. This can be formally achieved by a redefinition of the parton density functions (PDFs) at

NLO QED as follows [40, 43, 44],

$$f_{a/A}(x) \to f_{a/A}(x,\mu_F) + f_{a/A}(x,\mu_F)\,\frac{\alpha}{\pi}\,e_q^2\,\kappa_{\rm soft}^{\rm PDF} + \frac{\alpha}{\pi}\,e_q^2 \int_x^{1-\delta_s} \frac{dz}{z}\, f_{a/A}\Big(\frac{x}{z},\mu_F\Big)\,\kappa_{\rm coll}^{\rm PDF}(z) \tag{3.18}$$

$$\begin{aligned}
\text{with}\qquad \kappa_{\rm soft}^{\rm PDF} =& -1 + \ln\delta_s + \ln^2\delta_s - \ln\left(\frac{\mu_F^2}{m_q^2}\right)\left[\frac{3}{4} + \ln\delta_s\right]\\
&+ \frac{1}{4}\lambda_{\rm sc}\left[9 + \frac{2\pi^2}{3} + 3\ln\delta_s - 2\ln^2\delta_s\right],\\
\kappa_{\rm coll}^{\rm PDF}(z) =& \frac{1}{2}P_{qq}(z)\left[\ln\left(\frac{m_q^2\,(1-z)^2}{\mu_F^2}\right) + 1\right]\\
&- \frac{1}{2}\lambda_{\rm sc}\left[P_{qq}(z)\ln\frac{1-z}{z} - \frac{3}{2}\frac{1}{1-z} + 2z + 3\right].
\end{aligned}$$

The QED factorization scheme dependent $\lambda_{\rm sc}$-parameter is $\lambda_{\rm sc} = 0$ in the $\overline{MS}$-scheme and $\lambda_{\rm sc} = 1$ in the DIS scheme.

At the hadronic level, we define the collinear part of the real corrections for the case where parton a radiates off a collinear photon, in the following way by use of eq. (3.18),

$$\begin{aligned}
d\sigma_{\rm coll}(S) =& \frac{\alpha}{\pi}\,e_q^2 \int d\tau \int\frac{dx}{x}\int_x^{1-\delta_s}\frac{dz}{z}\,d\hat{\sigma}_0^{q\bar{q}}(\hat{s})\left[\kappa_{\rm coll}(z) + \kappa_{\rm coll}^{\rm PDF}(z)\right]\\
&\times\left[f_{a/A}\Big(\frac{x}{z},\mu_F\Big)\,f_{b/B}\Big(\frac{\tau}{x},\mu_F\Big) + f_{b/A}\Big(\frac{\tau}{x},\mu_F\Big)\,f_{a/B}\Big(\frac{x}{z},\mu_F\Big)\right],
\end{aligned} \tag{3.19}$$

where the lower limit of the z-integration is constrained to x, since the parton momentum fraction x/z has to be smaller than unity. The integral is free of any mass singularity,

$$\begin{aligned}
\kappa_{\rm coll}(z) + \kappa_{\rm coll}^{\rm PDF}(z) =& \frac{1}{2}P_{qq}(z)\,\ln\left(\frac{\hat{s}}{z}\frac{(1-z)^2}{\mu_F^2}\frac{\delta_\theta}{2}\right)\\
&+ \frac{1}{2}(1-z) - \frac{1}{2}\lambda_{\rm sc}\left[P_{qq}(z)\ln\frac{1-z}{z} - \frac{3}{2}\frac{1}{1-z} + 2z + 3\right].
\end{aligned} \tag{3.20}$$

The $\kappa_{\rm soft}^{\rm PDF}$-term in eq. (3.18) cancels the mass singularities owing to soft photons that remain in the sum of the virtual corrections and the soft correction factor $\delta_{\rm soft}^{\rm in}$ in eq. (3.13).

3.3 Photon-induced top-squark pair production

We also consider the photon-induced mechanisms of the top-squark pair production. At the hadronic level, these processes vanish at leading order owing to the non-existence of a photon distribution inside the proton. At NLO in QED, however, a non-zero photon density arises in the proton as a direct consequence of including higher order QED effects into the evolution of PDFs, leading thus to non-zero photon-induced hadronic contributions.

Feynman diagrams corresponding to the photon-gluon partonic process are illustrated in figure 18. Although these are contributions of different orders, they are tree-level contributions to the same hadronic final state and thus deserve a closer inspection. The differential cross section for this subprocess is

$$
\begin{aligned}
d\hat{\sigma}_0^{g\gamma}(\hat{s}) &= \frac{1}{16\pi\hat{s}^2}\overline{\sum}\left|\mathcal{M}_0^{g\gamma}(\hat{s},\hat{t}_r,\hat{u}_r)\right|^2 d\hat{t}\ , \\
\overline{\sum}\left|\mathcal{M}_0^{g\gamma}\right|^2 &= \frac{1}{4}\cdot\frac{1}{8}\cdot 128\pi^2\alpha\alpha_s e_t^2\, NC_F\left[1-2\frac{\hat{s}m_{\tilde{t}_i}^2}{\hat{t}_r\,\hat{u}_r}\left(1-\frac{\hat{s}m_{\tilde{t}_i}^2}{\hat{t}_r\,\hat{u}_r}\right)\right],
\end{aligned}
\tag{3.21}
$$

expressed in terms of the reduced Mandelstam variables $\hat{t}_r = \hat{t} - m_{\tilde{t}_i}^2$, $\hat{u}_r = \hat{u} - m_{\tilde{t}_i}^2$. The quark-photon partonic processes represent contributions of higher order and we do not include them in our discussion here.

The photon density is part of the PDFs at NLO QED, which have become available only recently [45]; here we present the first study of these effects on the top-squark pair production.

4. Numerical results

For the numerical discussion we focus on the production of light top-squark pairs $\tilde{t}_1^*\tilde{t}_1$ in proton-proton collisions for LHC energies. We present the results in terms of the following hadronic observables: the integrated cross section, σ, the differential cross section with respect to the (photon inclusive) invariant mass of the top-squark pair, $(d\sigma/dM_{\rm inv})$, the differential cross sections with respect to the transverse momentum, $(d\sigma/dp_T)$, to the rapidity, $(d\sigma/dy)$, and to the pseudo-rapidity, $(d\sigma/d\eta)$, of one of the final state top-squarks. For getting experimentally more realistic results for the cross sections we also apply typical sets of kinematical cuts. A study of the dependence on the various SUSY parameters is given towards the end of this section.

The NLO differential cross section at the hadron level is combined from the contributing partonic cross sections by convolution and summation as follows,

$$
d\sigma^{pp}(S) = \int_{\tau_0}^{1} d\tau\left\{\sum_i \frac{d\mathcal{L}_{q_i\bar{q}_i}^{pp}}{d\tau}\, d\hat{\sigma}^{q_i\bar{q}_i}(\hat{s}) + \frac{d\mathcal{L}_{gg}^{pp}}{d\tau}\, d\hat{\sigma}^{gg}(\hat{s}) + \frac{d\mathcal{L}_{g\gamma}^{pp}}{d\tau}\, d\hat{\sigma}_0^{g\gamma}(\hat{s})\right\}, \tag{4.1}
$$

where $d\hat{\sigma}^{q_i\bar{q}_i}$ and $d\hat{\sigma}^{gg}$ represent full one-loop results, including complete virtual and real corrections, and $d\hat{\sigma}_0^{g\gamma}$ is given in eq. (3.21). The respective parton luminosities refer to eq. (2.11).

One has to take care of the fact that each top-squark observed in the laboratory system under a certain angle θ can originate from two different constellations at parton level: parton $a(b)$ out of hadron $A(B)$ and vice-versa, corresponding to $\theta \to (\pi - \theta)$. Both parton level configurations have to be added correctly for hadronic distributions (for explicit formulas see e. g. [46]). Note that the two boost factors β relating the two partonic center-of-mass (c. m.) systems with the laboratory system differ by a relative sign, as do the rapidity and the pseudo-rapidity of each particle.

Assuming that the forward-scattered parton a carries the momentum fraction x of hadron A and the backward-scattered parton b the momentum fraction τ/x of hadron B, the boost factor β is given by

$$\beta = \frac{x - \tau/x}{x + \tau/x}\,. \tag{4.2}$$

The rapidity of one of the final state top-squarks in the laboratory system, $y(\equiv y_{\tilde{t}_1^*})$, is related to the rapidity in the partonic c. m. frame, $y^{\rm cm} = \operatorname{artanh}(p_z^{\rm cm}/E^{\rm cm})$, via a Lorentz transformation,

$$y = y^{\rm cm} - \operatorname{artanh}(-\beta) = y^{\rm cm} + \frac{1}{2}\ln\frac{x^2}{\tau}\,. \tag{4.3}$$

The pseudo-rapidity η is related to $\eta^{\rm cm} = -\ln(\tan\theta^{\rm cm}/2)$ in the c.m. frame via

$$\eta = \operatorname{arsinh}\left(\frac{1}{2}\sqrt{\frac{m_{\tilde{t}_1}^2}{p_T^2} + \cosh^2\eta^{\rm cm}}\left(\frac{x}{\sqrt{\tau}} - \frac{\sqrt{\tau}}{x}\right) + \frac{1}{2}\sinh\eta^{\rm cm}\left(\frac{\sqrt{\tau}}{x} + \frac{x}{\sqrt{\tau}}\right)\right), \tag{4.4}$$

which can be derived using the representation

$$p = \left(\sqrt{m_{\tilde{t}_1}^2 + p_T^2\cosh^2\eta},\, 0,\, p_T,\, p_T\sinh\eta\right) \tag{4.5}$$

for the top-squark momentum $p \equiv p_{\tilde{t}_1^*}$. Since the final state particles are massive, rapidity and pseudo-rapidity do not coincide; in the limit $m \to 0$ one obtains $\eta = y$.

4.1 Input parameters and conventions

Our Standard Model input parameters are chosen in correspondance with [47],

$$\begin{gathered} M_Z = 91.1876\,\text{GeV},\ M_W = 80.403\,\text{GeV}, \\ \alpha^{-1} = 137.036,\ \alpha(M_Z)^{-1} = 127.934,\ G_F = 1.1664\times 10^{-5}\,\text{GeV}^{-2}, \\ m_t = 172.7\,\text{GeV},\ m_b = 4.7\,\text{GeV},\ m_b(m_b) = 4.2\,\text{GeV}\,. \end{gathered} \tag{4.6}$$

All lepton and all other quark masses are set to zero unless where they are used for regularization. As a reference we consider the SPA SUSY parameter point SPS 1a' [47], unless stated otherwise. The current value of the top-quark mass, $m_t = 170.9 \pm 1.9\,\text{GeV}$ [48], increases the top-squark mass $m_{\tilde{t}_1}$ by 0.2%, which reduces the total cross section by $\approx 1\%$. The changes for the relative corrections are completely negligible.

For the parton distributions, we use the set MRST 2004 QED [45], as already mentioned previously. Factorization and renormalization scales are chosen equal, $\mu_F = \mu_R = 2m_{\tilde{t}_1}$. A study of the remaining QED-based scale dependence is not possible at the present stage since the QED and QCD evolution are not separated in the available parton densities. The scale dependence cannot be checked in a consistent way owing to the NLO QCD effects in the parton densities, which are not included in our calculation. For this reason we do not present a study of the scale dependence here. An important next step in improving the theoretical predictions would be to combine the NLO electroweak and QCD corrections.

As discussed above in section 3.2, the treatment of the IR singular bremsstrahlung is done using the phase space slicing method. We illustrate the method and its stability

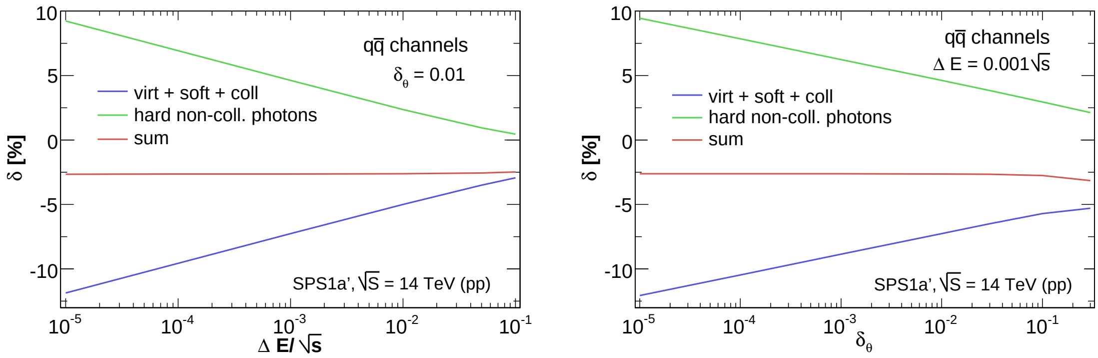

Figure 1: Dependence of the relative hadronic corrections in the $q\overline{q}$ channel on the cut-off parameters ΔE (left, $\delta_\theta = 0.01$ fixed) and δ_θ (right, $\Delta E = 0.001\sqrt{\hat{s}}$ fixed). Shown are the partial contributions (virtual corrections plus soft and collinear parts and the hard, non-collinear part) and the sum of all contributions for top-squark pair production at the LHC within the SPS1a' scenario.

in terms of the more involved case of $q\overline{q}$ annihilation, where two cut-off parameters are needed. The photon/gluon phase space is split into a soft part ($E_{\gamma/g} < \Delta E$), a collinear part ($E_{\gamma/g} > \Delta E$ and $\cos\theta > 1 - \delta_\theta$, θ being the angle between the photon/gluon and the radiating fermion), and a hard, non-collinear part ($E_{\gamma/g} > \Delta E$ and $\cos\theta < 1 - \delta_\theta$). The cut-off parameters for the photon and for the gluon phase space are chosen to be equal. As shown in figure 1, the sum of all contributions does not depend on the parameters when they are small enough. This is in accordance with the discussion in section 3.2 that for small enough cut-off parameters the soft and collinear contributions can be treated approximately according to eq. (3.11), (3.12), (3.16), and (3.17), respectively. In the following numerical analysis, we use $\Delta E = 0.001\sqrt{\hat{s}}$ and $\delta_\theta = 0.01$.

4.2 Hadronic cross sections and distributions

In table 1 we show results for the cross section for top-squark pair production at the LHC within four different scenarios, chosen out of the SPS benchmark scenarios of the minimal SUGRA type [47, 49, 50]. The integrated hadronic cross sections at leading order, σ^{LO}, the absolute size of the EW corrections corresponding to the difference between the LO and NLO cross sections, $\Delta\sigma^{\mathrm{NLO}}$, and the relative corrections, δ, given as the ratio of NLO corrections to the respective LO contributions, are presented for the gg fusion, the $q\overline{q}$ annihilation, and the $g\gamma$ fusion channel separately. The $g\gamma$ channel contributes only at NLO. For the $q\overline{q}$ channel, also the numbers for the $\mathcal{O}(\alpha^2)$ pure electroweak Born level contributions are given in brackets. These are typically smaller by one order of magnitude compared to the EW NLO corrections.

In scenarios where the top-squark $\tilde{t}_1$ is of intermediate or high mass (as SPS 1a, SPS 1a', and SPS 2) the NLO contributions are below 1%. The corrections to the $q\overline{q}$ and the gg channels are negative, whereas the $g\gamma$ contribution is always positive and of the same size as the other corrections or even larger. The situation is different in scenarios where the top-squark is very light, i.e. lighter than half of m_{H^0}, the mass of the heavier neutral Higgs

scenario	channel	$\sigma^{\rm LO}$ [fb]		$\Delta\sigma^{\rm NLO}$ [fb]	$\delta = \frac{\Delta\sigma^{\rm NLO}}{\sigma^{\rm LO}}$
SPS 1a	$q\bar{q}$	222	(+0.985)	-9.71	-4.4%
($m_{\tilde{t}_1} = 376.2\,\text{GeV}$)	gg	1444		-15.4	-1.1%
	$g\gamma$			29.0	
	total	**1666**		**3.90**	**0.23%**
SPS 1a'	$q\bar{q}$	439	(+1.88)	-11.6	-2.6%
($m_{\tilde{t}_1} = 322.1\,\text{GeV}$)	gg	3292		-14.6	-0.44%
	$g\gamma$			58.5	
	total	**3731**		**32.3**	**0.87%**
SPS 2	$q\bar{q}$	1.17	(+0.00539)	-8.99×10^{-2}	-7.7%
($m_{\tilde{t}_1} = 1005.7\,\text{GeV}$)	gg	2.97		-3.07×10^{-2}	-1.0%
	$g\gamma$			15.5×10^{-2}	
	total	**4.14**		$\mathbf{3.44 \times 10^{-2}}$	**0.83%**
SPS 5	$q\bar{q}$	2900	(+10.2)	-13.3	-0.46%
($m_{\tilde{t}_1} = 203.8\,\text{GeV}$)	gg	31960		499	1.6%
	$g\gamma$			405	
	total	**34860**		**891**	**2.6%**

Table 1: Numerical results for the integrated cross sections for light top-squark pair production at the LHC within different SPS scenarios [47, 49, 50].

boson H^0, where a large fraction of the squarks appears through production and decay of H^0 particles. This is the case in the SPS 5 scenario [$m_{\tilde{t}_1} = 204\,\text{GeV}$, $m_{H^0} = 694\,\text{GeV}$ and $\Gamma(H^0) = 9.7\,\text{GeV}$ derived from `FeynHiggs` [36, 37]]. The electroweak contributions in the gg channel are positive and slightly larger than the $g\gamma$ fusion contribution.

The interplay of the three production channels is illustrated in figure 2 where the absolute EW contributions $\Delta\sigma$ per channel are shown as distributions with respect to p_T, $M_{\rm inv}$, y, or η. Owing to the alternating signs, compensations occur where in particular the $g\gamma$ channel plays an important role.

For realistic experimental analyses, cuts on the kinematically allowed phase space of the top-squarks have to be applied. They can be realized by a lower cut on the transverse momenta of the final-state particles to focus on high-p_T jets. Moreover, detectability of the final state particles requires a minimal angle between the particles and the beam axis. Therefore, we set a cut on the pseudo-rapidity of the top-squarks restricting the scattering angle θ to a central region. Two exemplary sets of cuts are applied in the following figures (figures 2 – 5),

$$\text{cuts 1:}\quad p_T \geq 150\,\text{GeV and } |\eta| \leq 2.5 \quad (\text{i.e. } 9.4^\circ \leq \theta \leq 170.6^\circ),$$
$$\text{cuts 2:}\quad p_T \geq 250\,\text{GeV and } |\eta| \leq 2.5\,.$$

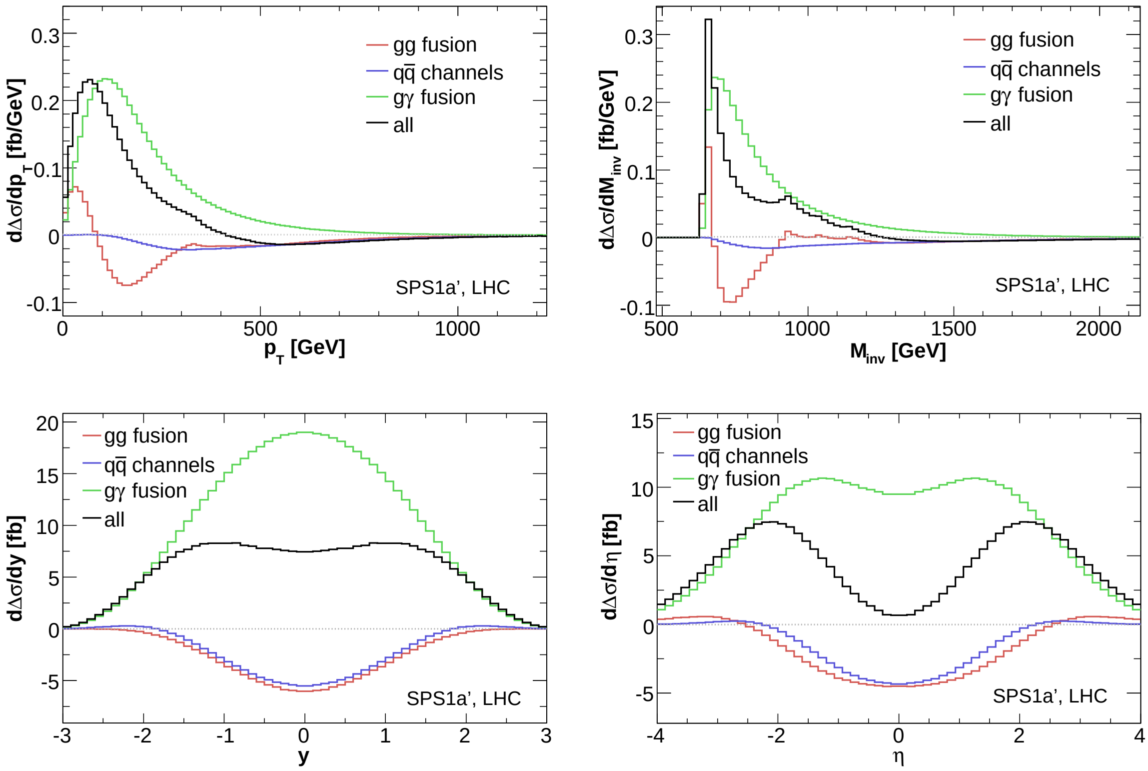

Figure 2: Comparison of EW NLO contributions from the various parton channels, for the distributions of transverse momentum $p_T(\tilde{t}_1^*)$, invariant mass of the stop pair, rapidity $y(\tilde{t}_1^*)$, and pseudo-rapidity $\eta(\tilde{t}_1^*)$ (from upper left to lower right). y and η are given in the laboratory frame. For gg fusion and $q\overline{q}$ annihilation, Δ denotes the difference between NLO and LO distributions ($\Delta\sigma \equiv \Delta\sigma^{\rm NLO}$), for $g\gamma$ one has $\Delta\sigma \equiv \sigma_0^{g\gamma}$.

channel (SPS 1a')	full result at NLO [fb]	$p_T < 150$ GeV & $\lvert\eta\rvert < 2.5$ [fb]	$p_T < 250$ GeV & $\lvert\eta\rvert < 2.5$ [fb]
gg	3280	1643 (−50%)	778 (−76%)
$q\overline{q}$	427	373 (−13%)	280 (−34%)
$g\gamma$	58.5	30.6 (−48%)	16.2 (−72%)

Table 2: Integrated hadronic cross section at NLO within the SPS 1a' scenario for the different production channels. Comparison of the full (unconstrained) results and cross sections where cuts on the pseudo-rapidities η and on the transverse momenta p_T of the outgoing top-squarks are applied. The relative changes compared to the full results are given in brackets.

The differential cross sections and the influence of cuts are the content of figures 3 and 4. Displayed are the hadronic cross sections at NLO, differential with respect to p_T, $M_{\rm inv}$ and to y, η, respectively. Both the full (unconstrained) distributions and the distributions with cuts applied are shown. The reduction of the integrated cross section owing to the application of cuts is summarized in table 2.

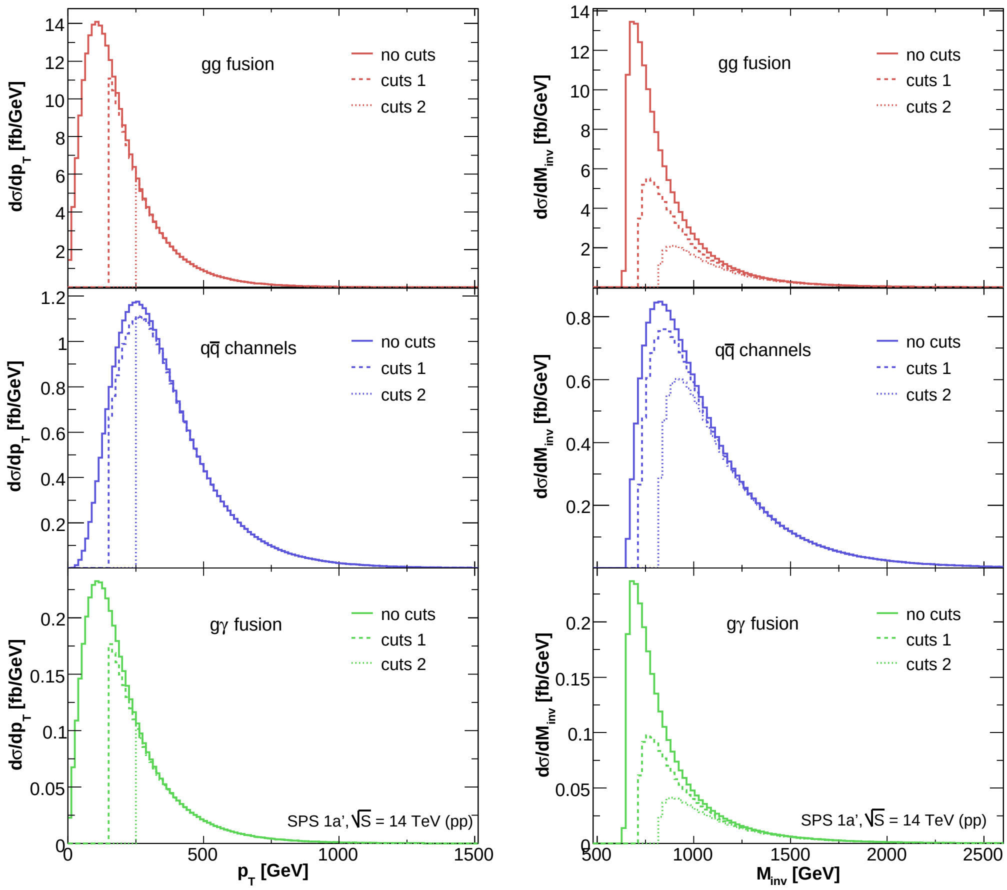

Figure 3: Comparison of EW NLO differential hadronic cross sections (solid lines) and the distributions where kinematical cuts on the final top-squarks are applied for all three production channels, gg fusion (upper red plots), $q\overline{q}$ channels (middle blue plots), and $g\gamma$ fusion (lower green plots). Cuts 1 (dashed lines): $\mathbf{p_T \geq 150\ GeV}$, $|\eta| \leq \mathbf{2.5}$, cuts 2 (dotted lines): $\mathbf{p_T \geq 250\ GeV}$, $|\eta| \leq \mathbf{2.5}$. Distributions with respect to the transverse momentum $p_T(\tilde{t}_1)$ (left) and the invariant mass of the stop pair (right) are shown for $\tilde{t}_1^* \tilde{t}_1$ pair production at the LHC within the SPS 1a' scenario.

The application of cuts reduces the gg and $g\gamma$ channels strongly, cutting off the peak of the p_T-distributions. The reduction is less pronounced in the $q\overline{q}$ channels where the p_T-distribution is harder. The p_T-cuts also shift the threshold of the invariant mass distributions towards higher values affecting again mainly the gg and $g\gamma$ channels in height and shape. The situation for the rapidity distribution is similar. In the $q\overline{q}$ channel, the harder p_T-distribution goes along with a narrower η-distribution, as shown in the right panels of figure 4. Most of the top-squarks produced via $q\overline{q}$ annihilation can be found in the central region. In contrast, top-squarks from gg or $g\gamma$ fusion are often produced in the strong forward (or backward) direction, and the application of cuts on the pseudo-rapidity thus reduces the number of gg or $g\gamma$ based events significantly.

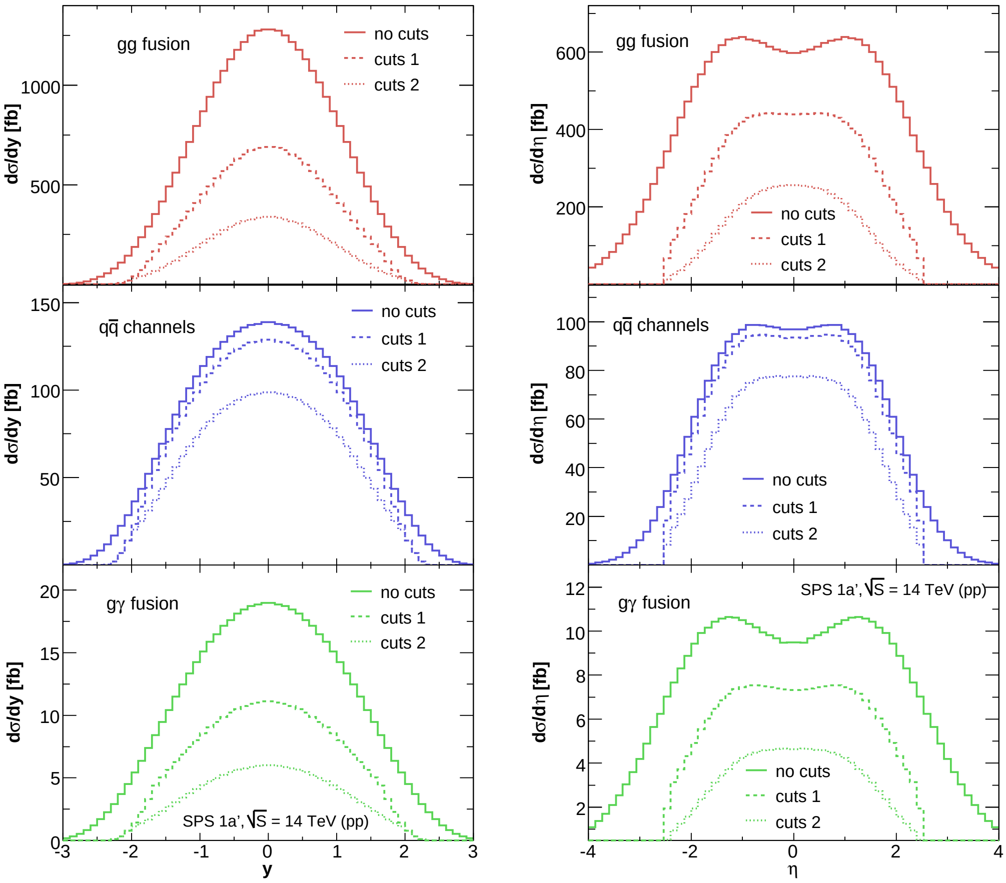

Figure 4: Same as figure 3, but with respect to the rapidity $y(\tilde{t}_1^*)$ (left) and the pseudo-rapidity $\eta(\tilde{t}_1^*)$ (right).

In order to illustrate the numerical impact of the NLO contributions on the LO cross section, we show in figure 5 K factors $K = \sigma^{\mathrm{NLO}}/\sigma^{\mathrm{LO}}$ for the gg and the $q\bar{q}$ channel, respectively, as distributions with respect to p_T and M_{inv}. The application of cuts influences the K factors only at low values of p_T and M_{inv}. The EW corrections in the p_T-distribution reach typically -10% in the gg channel, and -20% in the $q\bar{q}$ channel, for large values of p_T. In the invariant mass distributions, they are somewhat smaller, but still sizeable, at the 10% level for large M_{inv}. The large effects at high p_T and M_{inv} are dominated by the double logarithmic contributions arising from virtual W and Z bosons in loop diagrams.

The small peaks visible in the gg invariant mass distribution correspond to two-particle thresholds related to $\tilde{b}_1^*\tilde{b}_1$, $\tilde{b}_2^*\tilde{b}_2$, and $\tilde{t}_2^*\tilde{t}_2$ pairs in gg vertex and box diagrams, illustrated in figure 14 [in the SPS 1a' scenario, the masses of the involved squarks are $m_{\tilde{b}_1} = 460.7\,\mathrm{GeV}$, $m_{\tilde{b}_2} = 514.8\,\mathrm{GeV}$, $m_{\tilde{t}_2} = 569.4\,\mathrm{GeV}$]. Thresholds from the squarks of the first two generations are CKM suppressed. The threshold effects appear also in the p_T-distribution, around 300 GeV, but they are smeared out and much less pronounced.

Figure 6 shows total K factors, defined as $K = (\sigma_{gg}^{\mathrm{NLO}} + \sigma_{q\bar{q}}^{\mathrm{NLO}} + \sigma_{g\gamma}^{\mathrm{LO}})/(\sigma_{gg}^{\mathrm{LO}} + \sigma_{q\bar{q}}^{\mathrm{LO}})$. It is

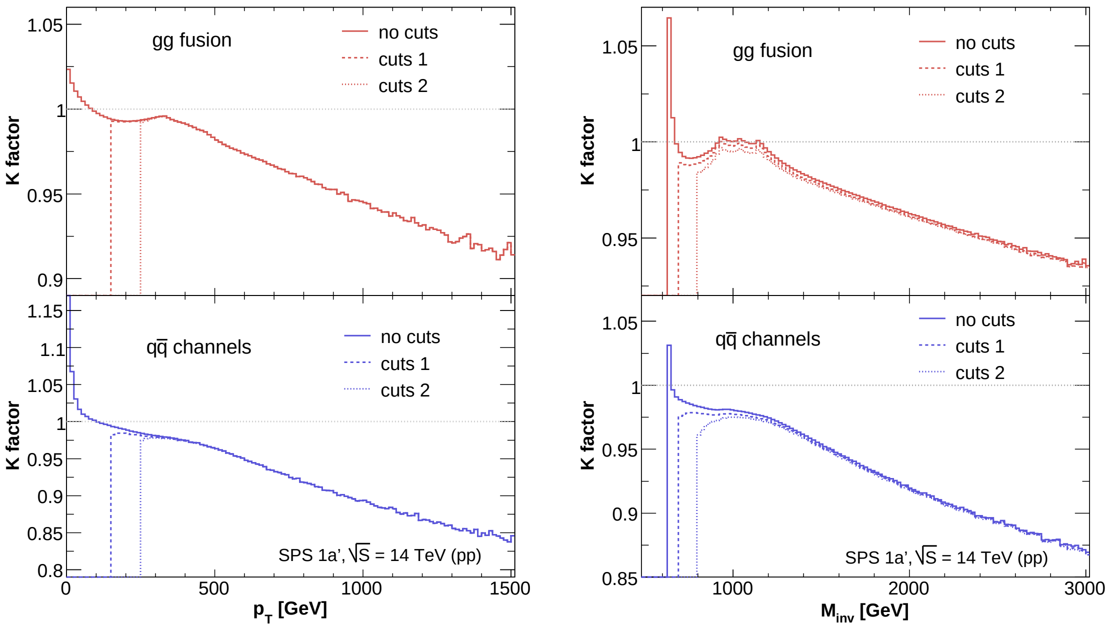

Figure 5: Same as figure 3, but shown are the K factors, $K = \sigma^{\rm NLO}/\sigma^{\rm LO}$, for gg fusion (upper plots) and $q\bar{q}$ channels (lower plots).

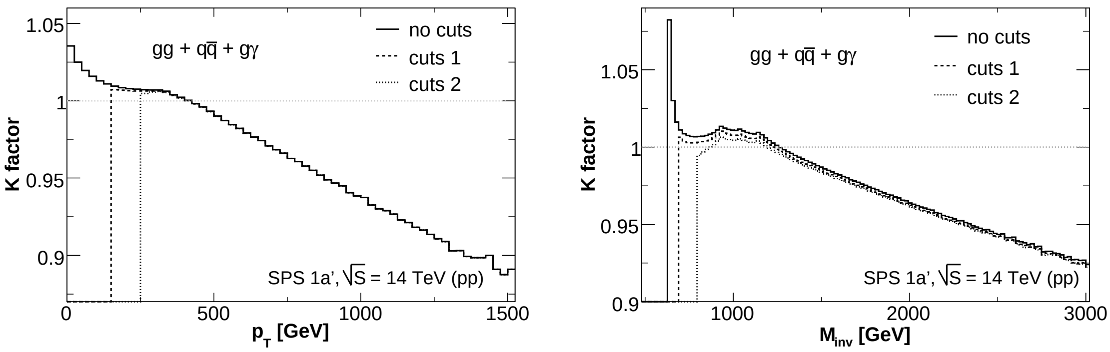

Figure 6: Same as figure 3, but shown is the total K factor, $K = (\sigma_{gg}^{\rm NLO}+\sigma_{q\bar{q}}^{\rm NLO}+\sigma_{g\gamma}^{\rm LO})/(\sigma_{gg}^{\rm LO}+\sigma_{q\bar{q}}^{\rm LO})$.

obvious that, although small for the total cross section, the EW higher order contributions cannot be neglected for differential distributions where, in the high-p_T and high-$M_{\rm inv}$ range, they are of the same order of magnitude as the SUSY-QCD corrections [21, 22].

4.3 SUSY parameter dependence

In order to study the dependence of the EW contributions on the various SUSY parameters in more detail, we consider the ratio of the NLO contribution in each channel to the combined $gg + q\bar{q}$ Born cross section, $\delta_{\rm tot} = \Delta\sigma^{\rm NLO}_{\{gg,\, q\bar{q},\, g\gamma\}}/\sigma^{\rm LO}_{\rm tot}$. We focus on those parameters

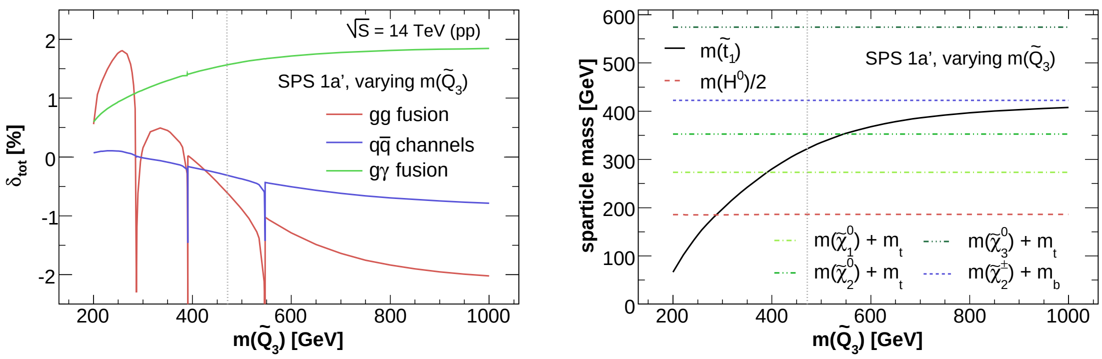

Figure 7: Left: Relative EW corrections as a function of the soft-breaking parameter $m_{\tilde{Q}_3}$ for each of the indicated channels compared to the combined $(gg + q\overline{q})$ LO cross section in the SPS 1a' scenario where $m_{\tilde{Q}_3}$ is varied around the SPS1a' value (gray dotted line). Right: Mass of $\tilde{t}_1$, half of the mass of H^0, sums of the masses of the top-quark and $\tilde{\chi}^0_1$, $\tilde{\chi}^0_2$, and $\tilde{\chi}^0_3$, respectively, and sum of the masses of the bottom-quark and $\tilde{\chi}^\pm_2$ as a function of $m_{\tilde{Q}_3}$. All other parameters are chosen according to the SPS1a' scenario.

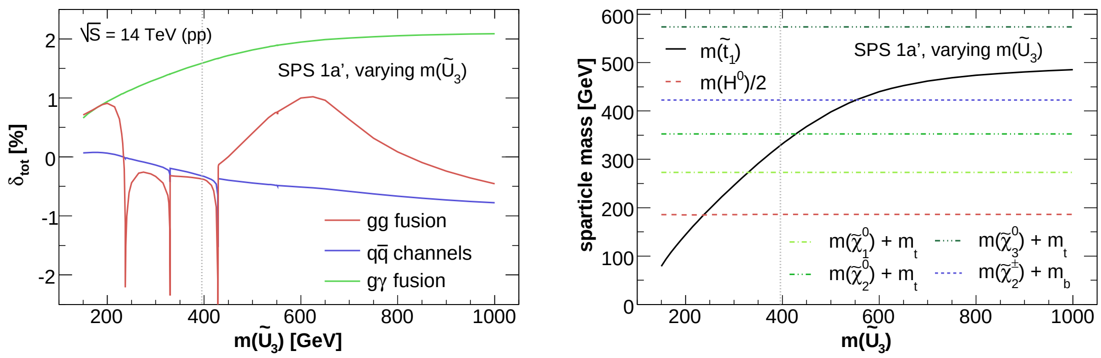

Figure 8: Same as figure 7, but for variation of the soft-breaking parameter $m_{\tilde{U}_3}$.

that determine the top-squark mass, cf. eq. (2.4), and vary each quantity out of the set $m_{\tilde{Q}_3}$, $m_{\tilde{U}_3}$, $\tan\beta$, A_t, or μ around its SPS 1a' value while keeping all other parameters fixed to those of the default SPS 1a' scenario. The results are displayed in the left panels of figures 7–11. Simultaneously, we show the mass of the light top-squark $\tilde{t}_1$ as a function of the varied parameter in the respective right panels (black solid lines). The parameter configuration of the SPS 1a' scenario is marked by a vertical gray dotted line in all the figures.

We find the following general behaviors. The $g\gamma$ contributions are from tree level diagrams and the only relevant parameter is thus the top-squark mass $m_{\tilde{t}_1}$. In all scenarios, the $g\gamma$ fusion channel is as important as the EW corrections to the $q\overline{q}$ and gg processes. The $q\overline{q}$ corrections, being practically always negative, involve many different SUSY particles in the loops, although the relative corrections show only small variations. The gg contributions are more sensitive to the considered SUSY parameters. The plots show strik-

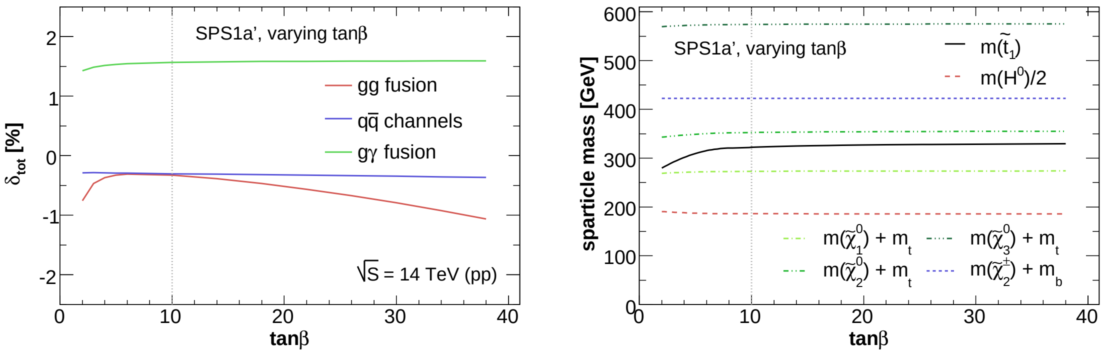

Figure 9: Same as figure 7, but for variation of $\tan\beta$.

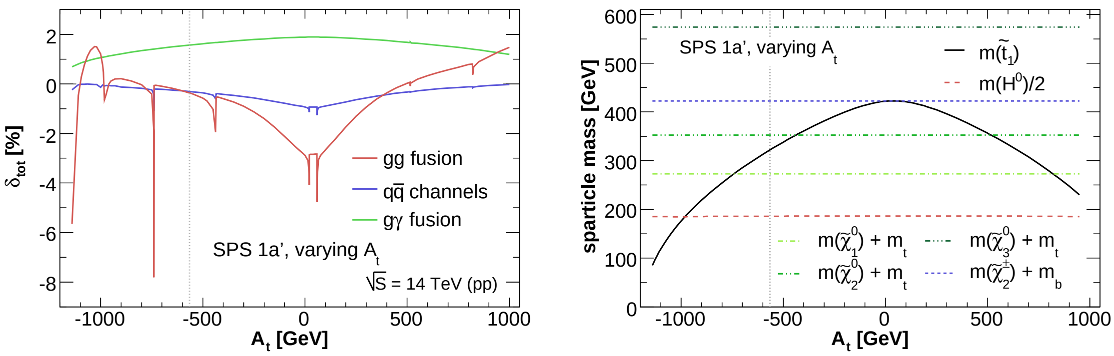

Figure 10: Same as figure 8, but for variation of trilinear coupling parameter A_t.

ing peaks (some of them are also visible in $q\bar{q}$ annihilation), which correspond to threshold effects and can be explained by the SUSY particle masses displayed at the right panels of figures 7 – 11. They occur in the Higgs-exchange diagrams when $m_{\tilde{t}_1} = m_{H^0}/2$ (red long-dashed lines in the figures), and in the top-squark wave function renormalization when $m_{\tilde{t}_1}$ equals the sum of masses of a neutralino and the top-quark (green dash-dotted lines) or of a chargino and the bottom-quark (blue dashed lines). The chargino-induced peaks are less pronounced than those from neutralinos and not visible in figure 8 and figure 11.

Outside of such singular parameter configurations, over a wide range of SUSY parameters, the combined EW contributions to top-squark pair production are only weakly parameter dependent.

5. Conclusions

We have completed the NLO calculation for the $\tilde{t}\tilde{t}^*$ production at hadron colliders by providing the complete EW corrections at the one-loop level.

To obtain a consistent and IR-finite result, we have considered the interference terms

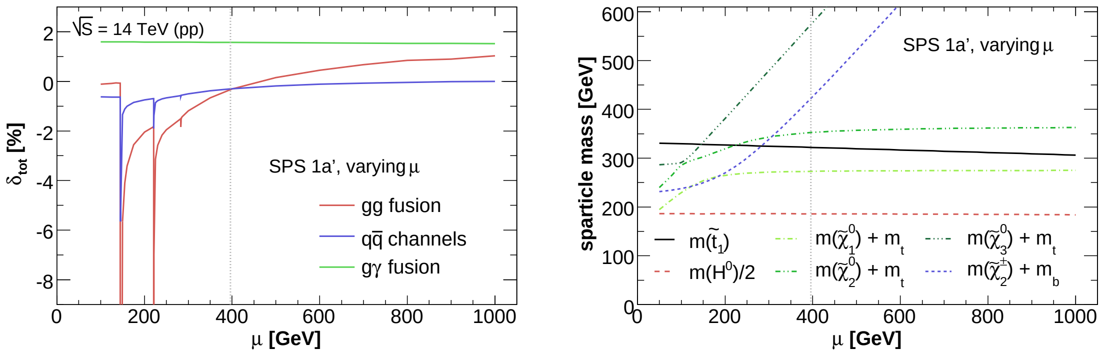

Figure 11: Same as figure 7, but for variation of the Higgs parameter μ.

between QCD and EW NLO terms for both virtual and real contributions. Also, a new class of photon-induced partonic processes of $\tilde{t}\tilde{t}^*$ production occurs, which was found to yield considerable contributions, comparable in size to the corrections to $q\overline{q}$ annihilation and gg fusion or even larger.

In total, the NLO EW contributions reach in size the $10 - 20\%$ level in the p_T and invariant-mass distributions and are thus significant. Outside singular parameter configurations associated with thresholds, the dependence on the MSSM parameters is rather smooth.

Recently, a preprint appeared on the same topic [51], where the authors consider virtual corrections and the soft part of the real corrections, both for the gg fusion channel; the hard part of the real corrections, as well as the contributions from the other channels are missing. The numerical results can therefore not directly be compared with ours at this stage.

Acknowledgments

The authors want to thank Tilman Plehn for helpful discussions and Edoardo Mirabella for cross-checking parts of the results.

A. Feynman diagrams

We show here generic Feynman Diagrams for the pair production of lighter top-squark at $\mathcal{O}(\alpha\alpha_s^2)$. Diagrams for $\tilde{t}_2^*\tilde{t}_2$ production can be constructed in complete analogy. The $q\bar{q}$ annihilation channels are exemplified by $u\bar{u}$ annihilation. Furthermore, the label S^0 refers to all neutral Higgs (and Goldstone) bosons h^0, H^0, A^0, G^0, and the label S to all charged Higgs (and Goldstone) bosons $H^{\pm}$, $G^{\pm}$.

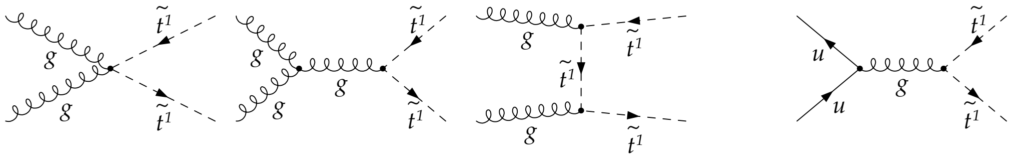

Figure 12: Feynman diagrams for top-squark pair production at the Born level via gg fusion (left) and $q\bar{q}$ annihilation (right), here shown for u-quarks. As in the following figures, diagrams with crossed final states are not shown explicitely.

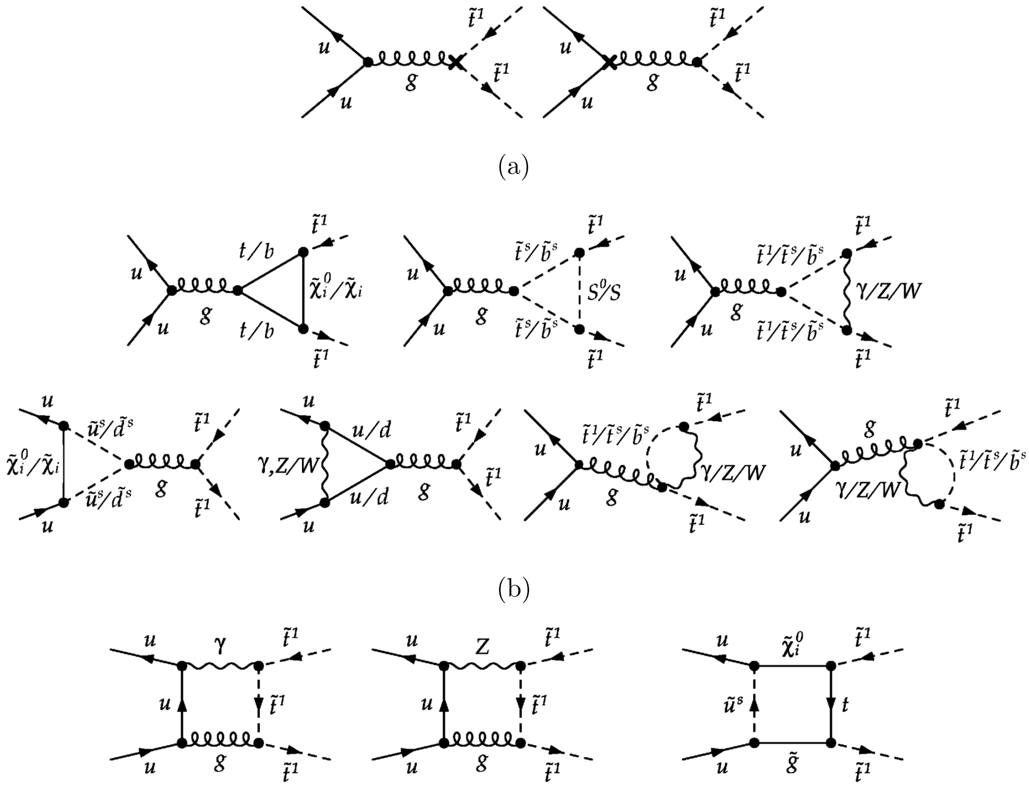

Figure 13: Feynman diagrams for virtual corrections to top-squark pair production via $q\bar{q}$ annihilation (here for u-quarks). The label S^0 refers to all neutral Higgs bosons h^0, H^0, A^0, G^0, the label S to all charged Higgs bosons $H^{\pm}$, $G^{\pm}$. (a) counter-term diagrams, (b) vertex corrections, (c) IR singular box diagrams, (d) IR finite box diagram.

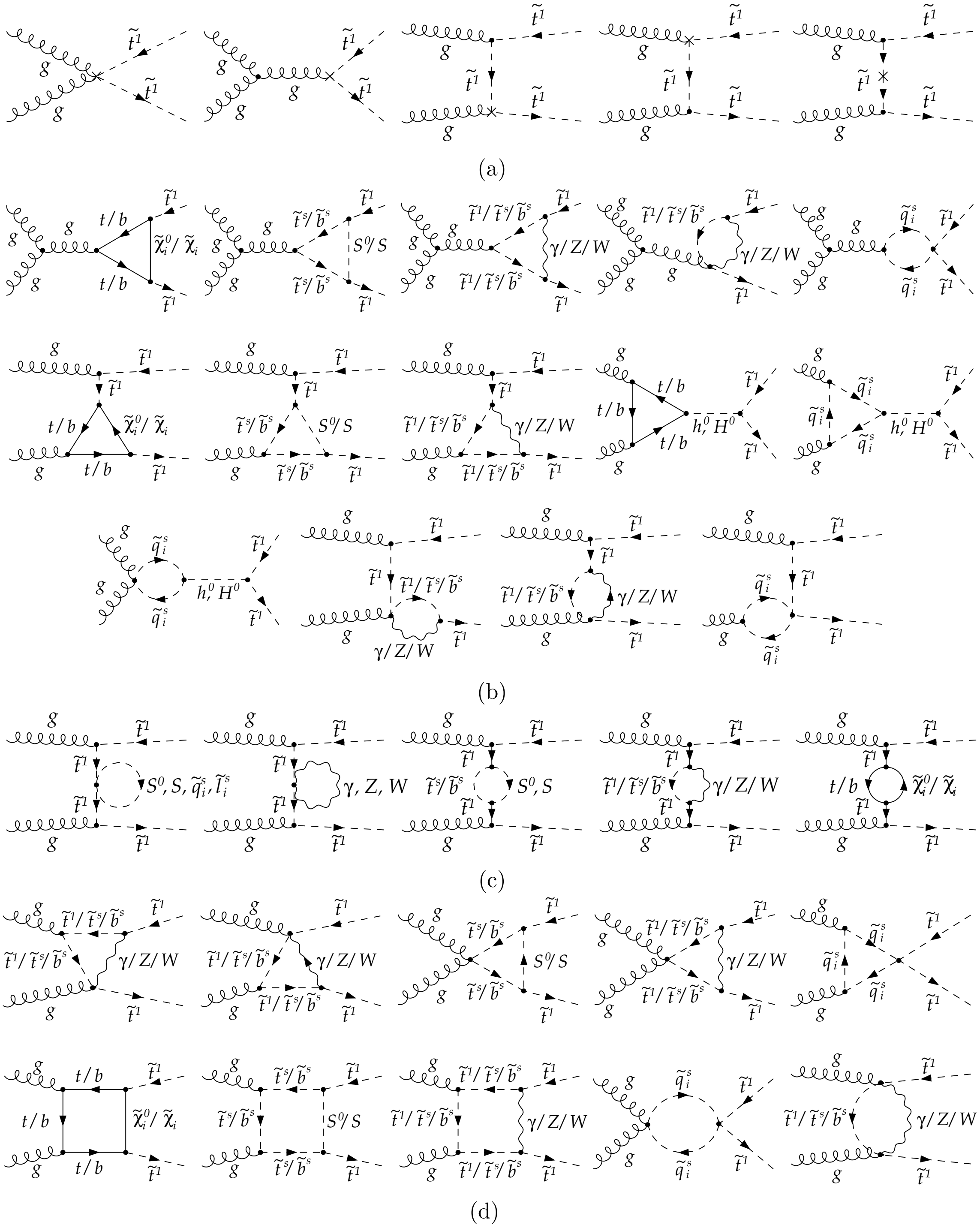

Figure 14: Feynman diagrams for virtual corrections to top-squark pair production via gg fusion, diagrams with crossed final states are not explicitely shown. The label S^0 refers to all neutral Higgs bosons h^0, H^0, A^0, G^0, the label S to all charged Higgs bosons $H^\pm$, $G^\pm$. (a) counter-term diagrams, (b) vertex corrections, (c) self-energy corrections, (d) box diagrams.

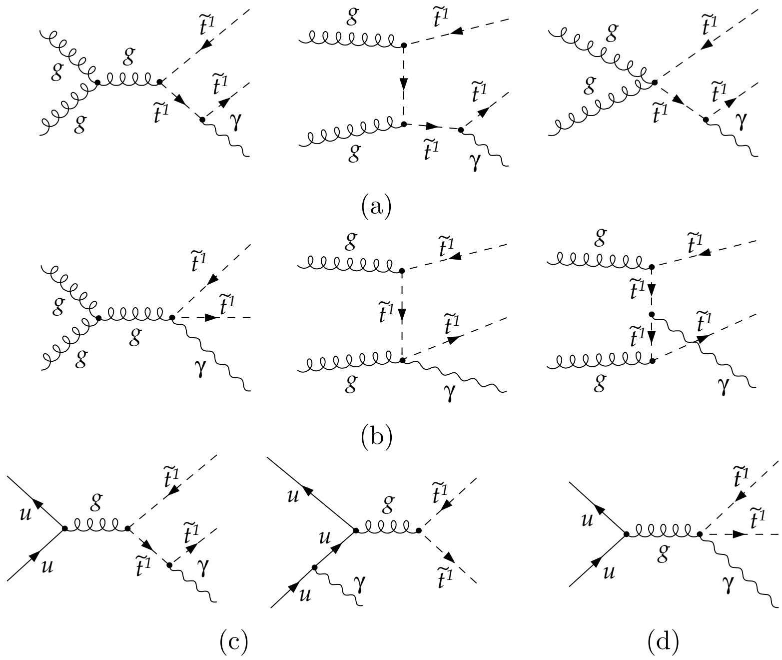

Figure 15: Feynman diagrams for real photon radiation. (a) IR divergent – (b) IR finite contributions for the gg channel; (c) IR divergent – (d) IR finite contributions for the $q\bar{q}$ channels. Feynman diagrams with photon radiation off the other quark or squark and with crossed final states are not shown explicitely.

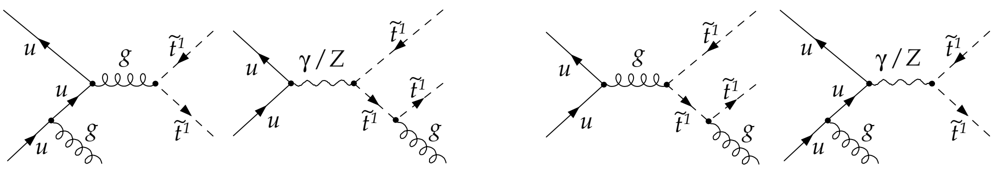

Figure 16: Feynman diagrams for gluon bremsstrahlung from the QCD and EW Born diagrams (radiation from upper legs is not explicitly shown). Only interference terms between initial and final state gluon radiation are non-vanishing.

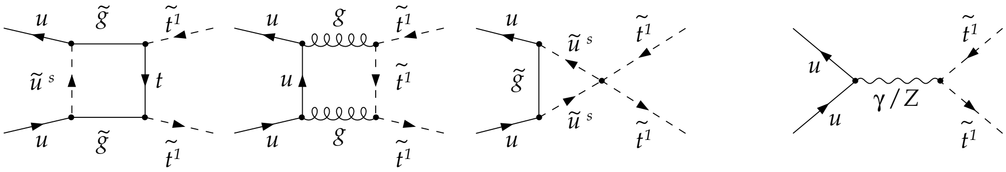

Figure 17: Feynman diagrams for box contributions of $\mathcal{O}(\alpha_s^2)$ (left) interfering with electroweak Born graphs (right), here for $u\bar{u}$ annihilation.

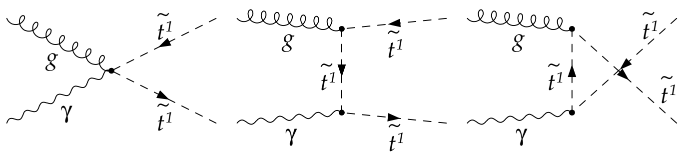

Figure 18: Feynman diagrams for gluon-photon fusion.

References

[1] J.R. Ellis and S. Rudaz, *Search for supersymmetry in toponium decays*, *Phys. Lett.* **B 128** (1983) 248.

[2] A. Djouadi, J. Kalinowski, P. Ohmann and P.M. Zerwas, *Heavy SUSY Higgs bosons at e^+e^- linear colliders*, *Z. Physik* **C 74** (1997) 93 [hep-ph/9605339].

[3] ALEPH collaboration, A. Heister et al., *Search for scalar quarks in e^+e^- collisions at $\sqrt{s}$ up to 209 GeV*, *Phys. Lett.* **B 537** (2002) 5 [hep-ex/0204036].

[4] DELPHI collaboration, P. Abreu et al., *Search for supersymmetric partners of top and bottom quarks at $\sqrt{s}$ = 189 GeV*, *Phys. Lett.* **B 496** (2000) 59 [hep-ex/0103034].

[5] L3 collaboration, M. Acciarri et al., *Searches for scalar quarks in e^+e^- interactions at $\sqrt{s}$ = 189 GeV*, *Phys. Lett.* **B 471** (1999) 308 [hep-ex/9910020].

[6] OPAL collaboration, G. Abbiendi et al., *Search for scalar top and scalar bottom quarks at LEP*, *Phys. Lett.* **B 545** (2002) 272 [hep-ex/0209026].

[7] A.C. Kraan, *Stop and sbottom searches at LEP*, hep-ex/0305051.

[8] CDF collaboration, A.A. Affolder et al., *Search for scalar top quark production in $p\bar{p}$ collisions at $\sqrt{s}$= 1.8 TeV*, *Phys. Rev. Lett.* **84** (2000) 5273 [hep-ex/9912018].

[9] D0 collaboration, V.M. Abazov et al., *Search for pair production of light scalar top quarks in $p\bar{p}$ collisions at $\sqrt{s}$ = 1.8 TeV*, *Phys. Rev. Lett.* **93** (2004) 011801 [hep-ex/0404028].

[10] CDF collaboration, T. Aaltonen et al., *Search for direct pair production of supersymmetric top and supersymmetric bottom quarks in $p\bar{p}$ collisions at $\sqrt{s}$= 1.96 TeV*, *Phys. Rev.* **D 76** (2007) 072010 [arXiv:0707.2567].

[11] D0 collaboration, V.M. Abazov et al., *Search for the pair production of scalar top quarks in the acoplanar charm jet topology in $p\bar{p}$ collisions at $\sqrt{s}$=1.96 TeV*, *Phys. Lett.* **B 645** (2007) 119 [hep-ex/0611003].

[12] D0 collaboration, V.M. Abazov et al., *Search for squarks and gluinos in events with jets and missing transverse energy in $p\bar{p}$ collisions at $\sqrt{s}$ = 1.96 TeV*, *Phys. Lett.* **B 638** (2006) 119 [hep-ex/0604029].

[13] CDF and D0 collaboration, T. Nunnemann, *Searches for scalar top and bottom quarks at the Tevatron*, PoS(HEP2005)348 [hep-ex/0602038].

[14] H1 collaboration, A. Aktas et al., *Search for bosonic stop decays in R-parity violating supersymmetry in e^+ p collisions at HERA*, *Phys. Lett.* **B 599** (2004) 159 [hep-ex/0405070].

[15] ZEUS collaboration, *Search for stop production in R-parity-violating supersymmetry at HERA*, *Eur. Phys. J.* **C 50** (2007) 269 [hep-ex/0611018].

[16] G.L. Kane and J.P. Leveille, *Experimental constraints on gluino masses and supersymmetric theories*, *Phys. Lett.* **B 112** (1982) 227.

[17] P.R. Harrison and C.H. Llewellyn Smith, *Hadroproduction of supersymmetric particles*, *Nucl. Phys.* **B 213** (1983) 223.

[18] E. Reya and D.P. Roy, *Supersymmetric particle production at $p\bar{p}$ collider energies*, *Phys. Rev.* **D 32** (1985) 645.

JHEP02(2008)018

[19] S. Dawson, E. Eichten and C. Quigg, *Search for supersymmetric particles in hadron-hadron collisions*, *Phys. Rev.* **D 31** (1985) 1581.

[20] H. Baer and X. Tata, *Component formulae for hadroproduction of left-handed and right-handed squarks*, *Phys. Lett.* **B 160** (1985) 159.

[21] W. Beenakker, R. Höpker, M. Spira and P.M. Zerwas, *Squark production at the Tevatron*, *Phys. Rev. Lett.* **74** (1995) 2905 [hep-ph/9412272].

[22] W. Beenakker, R. Höpker, M. Spira and P.M. Zerwas, *Squark and gluino production at hadron colliders*, *Nucl. Phys.* **B 492** (1997) 51 [hep-ph/9610490].

[23] W. Beenakker, M. Krämer, T. Plehn, M. Spira and P.M. Zerwas, *Stop production at hadron colliders*, *Nucl. Phys.* **B 515** (1998) 3 [hep-ph/9710451].

[24] G. Bozzi, B. Fuks and M. Klasen, *Non-diagonal and mixed squark production at hadron colliders*, *Phys. Rev.* **D 72** (2005) 035016 [hep-ph/0507073].

[25] A. Bartl et al., *Search of stop, sbottom, tau-sneutrino and stau at an e^+e^- linear collider with $\sqrt{s}$=0.5 TeV to 2 TeV*, *Z. Physik* **C 76** (1997) 549 [hep-ph/9701336].

[26] H.E. Haber and G.L. Kane, *The search for supersymmetry: probing physics beyond the standard model*, *Phys. Rept.* **117** (1985) 75.

[27] J. Küblbeck, M. Böhm and A. Denner, *FeynArts: Computer algebraic generation of Feynman graphs and amplitudes*, *Comput. Phys. Commun.* **60** (1990) 165.

[28] T. Hahn, *Generating Feynman diagrams and amplitudes with FeynArts* 3, *Comput. Phys. Commun.* **140** (2001) 418 [hep-ph/0012260].

[29] T. Hahn and C. Schappacher, *The implementation of the minimal supersymmetric standard model in FeynArts and FormCalc*, *Comput. Phys. Commun.* **143** (2002) 54 [hep-ph/0105349].

[30] T. Hahn and M. Pérez-Victoria, *Automatized one-loop calculations in four and D dimensions*, *Comput. Phys. Commun.* **118** (1999) 153 [hep-ph/9807565].

[31] T. Hahn and M. Rauch, *News from FormCalc and LoopTools*, *Nucl. Phys.* **157** *(Proc. Suppl.)* (2006) 236 [hep-ph/0601248].

[32] G. 't Hooft and M.J.G. Veltman, *Scalar one loop integrals*, *Nucl. Phys.* **B 153** (1979) 365.

[33] G. Passarino and M.J.G. Veltman, *One loop corrections for e^+e^- annihilation into $\mu^+\mu^-$ in the Weinberg model*, *Nucl. Phys.* **B 160** (1979) 151.

[34] W. Beenakker and A. Denner, *Infrared divergent scalar box integrals with applications in the electroweak standard model*, *Nucl. Phys.* **B 338** (1990) 349.

[35] A. Denner, U. Nierste and R. Scharf, *A compact expression for the scalar one loop four point function*, *Nucl. Phys.* **B 367** (1991) 637.

[36] S. Heinemeyer, W. Hollik and G. Weiglein, *FeynHiggs: a program for the calculation of the masses of the neutral CP-even Higgs bosons in the MSSM*, *Comput. Phys. Commun.* **124** (2000) 76 [hep-ph/9812320].

[37] T. Hahn et al., *Higher-order corrected Higgs bosons in FeynHiggs* 2.5, *Pramana* **69** (2007) 861 [hep-ph/0611373].

JHEP02(2008)018

[38] F. Bloch and A. Nordsieck, *Note on the radiation field of the electron*, *Phys. Rev.* **52** (1937) 54.

[39] W. Beenakker, S.C. van der Marck and W. Hollik, *e^+e^- annihilation into heavy fermion pairs at high-energy colliders*, *Nucl. Phys.* **B 365** (1991) 24.

[40] U. Baur, S. Keller and D. Wackeroth, *Electroweak radiative corrections to W boson production in hadronic collisions*, *Phys. Rev.* **D 59** (1999) 013002 [hep-ph/9807417].

[41] S. Dittmaier and M. Krämer, *Electroweak radiative corrections to W-boson production at hadron colliders*, *Phys. Rev.* **D 65** (2002) 073007 [hep-ph/0109062].

[42] G. Altarelli and G. Parisi, *Asymptotic freedom in parton language*, *Nucl. Phys.* **B 126** (1977) 298.

[43] D. Wackeroth and W. Hollik, *Electroweak radiative corrections to resonant charged gauge boson production*, *Phys. Rev.* **D 55** (1997) 6788 [hep-ph/9606398].

[44] K.P.O. Diener, S. Dittmaier and W. Hollik, *Electroweak radiative corrections to deep-inelastic neutrino scattering: implications for NuTeV?*, *Phys. Rev.* **D 69** (2004) 073005 [hep-ph/0310364].

[45] A.D. Martin, R.G. Roberts, W.J. Stirling and R.S. Thorne, *Parton distributions incorporating QED contributions*, *Eur. Phys. J.* **C 39** (2005) 155 [hep-ph/0411040].

[46] O. Brein and W. Hollik, *Distributions for MSSM Higgs boson + jet production at hadron colliders*, *Phys. Rev.* **D 76** (2007) 035002 [arXiv:0705.2744].

[47] J.A. Aguilar-Saavedra et al., *Supersymmetry parameter analysis: SPA convention and project*, *Eur. Phys. J.* **C 46** (2006) 43 [hep-ph/0511344].

[48] See http://www-cdf.fnal.gov/physics/new/top/top.html.

[49] B.C. Allanach et al., *The Snowmass points and slopes: benchmarks for SUSY searches*, hep-ph/0202233.

[50] http://www.ippp.dur.ac.uk/~georg/sps/sps.html.

[51] M. Beccaria, G. Macorini, L. Panizzi, F.M. Renard and C. Verzegnassi, *A survey of one-loop electroweak supersymmetric effects in stop-antistop production at LHC*, arXiv:0710.5357.